Phase-stabilized optical frequency domain imaging at 1-mu m for the measurement of blood flow in the human choroid

Braaf, B.; Vermeer, K.A.; Sicam, V.A.D.P.; Zeeburg, E.; van Meurs, J.C.; de Boer, J.F.

published in
Optics Express
2011

DOI (link to publisher)
10.1364/OE.19.020886

document version
Publisher's PDF, also known as Version of record

Phase-stabilized optical frequency domain imaging at 1-µm for the measurement of blood flow in the human choroid

Boy Braaf,[1,*] Koenraad A. Vermeer,[1] Victor Arni D.P. Sicam,[1] Elsbeth van Zeeburg,[1,2] Jan C. van Meurs,[2] and Johannes F. de Boer[1,3]

[1]*Rotterdam Ophthalmic Institute, Schiedamse Vest 160, 3011 BH Rotterdam, The Netherlands*
[2]*The Rotterdam Eye Hospital, Schiedamse Vest 180, 3011 BH Rotterdam, The Netherlands*
[3]*Institute for Lasers, Life and Biophotonics Amsterdam, Department of Physics and Astronomy, VU University, de Boelelaan 1081, 1081 HV Amsterdam, The Netherlands*
[*]*b.braaf@eyehospital.nl*

Abstract: In optical frequency domain imaging (OFDI) the measurement of interference fringes is not exactly reproducible due to small instabilities in the swept-source laser, the interferometer and the data-acquisition hardware. The resulting variation in wavenumber sampling makes phase-resolved detection and the removal of fixed-pattern noise challenging in OFDI. In this paper this problem is solved by a new post-processing method in which interference fringes are resampled to the exact same wavenumber space using a simultaneously recorded calibration signal. This method is implemented in a high-speed (100 kHz) high-resolution (6.5 µm) OFDI system at 1-µm and is used for the removal of fixed-pattern noise artifacts and for phase-resolved blood flow measurements in the human choroid. The system performed close to the shot-noise limit (<1dB) with a sensitivity of 99.1 dB for a 1.7 mW sample arm power. Suppression of fixed-pattern noise artifacts is shown up to 39.0 dB which effectively removes all artifacts from the OFDI-images. The clinical potential of the system is shown by the detection of choroidal blood flow in a healthy volunteer and the detection of tissue reperfusion in a patient after a retinal pigment epithelium and choroid transplantation.

OCIS codes: (110.0110) Imaging systems; (170.3880) Medical and biological imaging; (110.4500) Optical coherence tomography; (170.4470) Ophthalmology; (280.2490) Flow diagnostics.

References and links

1. D. Huang, E. A. Swanson, C. P. Lin, J. S. Schuman, W. G. Stinson, W. Chang, M. R. Hee, T. Flotte, K. Gregory, C. A. Puliafito, and J. G. Fujimoto, "Optical coherence tomography," Science **254**(5035), 1178–1181 (1991).
2. J. F. de Boer, B. Cense, B. H. Park, M. C. Pierce, G. J. Tearney, and B. E. Bouma, "Improved signal-to-noise ratio in spectral-domain compared with time-domain optical coherence tomography," Opt. Lett. **28**(21), 2067–2069 (2003).
3. R. Leitgeb, C. Hitzenberger, and A. Fercher, "Performance of fourier domain vs. time domain optical coherence tomography," Opt. Express **11**(8), 889–894 (2003).
4. M. Choma, M. Sarunic, C. Yang, and J. Izatt, "Sensitivity advantage of swept source and Fourier domain optical coherence tomography," Opt. Express **11**(18), 2183–2189 (2003).
5. N. Nassif, B. Cense, B. Park, M. Pierce, S. Yun, B. Bouma, G. Tearney, T. Chen, and J. de Boer, "In vivo high-resolution video-rate spectral-domain optical coherence tomography of the human retina and optic nerve," Opt. Express **12**(3), 367–376 (2004).
6. A. F. Fercher, C. K. Hitzenberger, G. Kamp, and S. Y. Elzaiat, "Measurement of intraocular distances by backscattering spectral interferometry," Opt. Commun. **117**(1-2), 43–48 (1995).
7. S. R. Chinn, E. A. Swanson, and J. G. Fujimoto, "Optical coherence tomography using a frequency-tunable optical source," Opt. Lett. **22**(5), 340–342 (1997).
8. S. Yun, G. Tearney, J. de Boer, N. Iftimia, and B. Bouma, "High-speed optical frequency-domain imaging," Opt. Express **11**(22), 2953–2963 (2003).
9. S. H. Yun, G. Tearney, J. de Boer, and B. Bouma, "Motion artifacts in optical coherence tomography with frequency-domain ranging," Opt. Express **12**(13), 2977–2998 (2004).

#150555 - $15.00 USD Received 5 Jul 2011; revised 10 Sep 2011; accepted 17 Sep 2011; published 5 Oct 2011

10. J. W. You, T. C. Chen, M. Mujat, B. H. Park, and J. F. de Boer, "Pulsed illumination spectral-domain optical coherence tomography for human retinal imaging," Opt. Express **14**(15), 6739–6748 (2006).
11. W. Drexler, U. Morgner, R. K. Ghanta, F. X. Kartner, J. S. Schuman, and J. G. Fujimoto, "Ultrahigh-resolution ophthalmic optical coherence tomography," Nat. Med. **7**(4), 502–507 (2001).
12. A. Unterhuber, B. Povazay, B. Hermann, H. Sattmann, A. Chavez-Pirson, and W. Drexler, "In vivo retinal optical coherence tomography at 1040 nm - enhanced penetration into the choroid," Opt. Express **13**(9), 3252–3258 (2005).
13. E. C. Lee, J. F. de Boer, M. Mujat, H. Lim, and S. H. Yun, "In vivo optical frequency domain imaging of human retina and choroid," Opt. Express **14**(10), 4403–4411 (2006).
14. Y. Chen, D. L. Burnes, M. de Bruin, M. Mujat, and J. F. de Boer, "Three-dimensional pointwise comparison of human retinal optical property at 845 and 1060 nm using optical frequency domain imaging," J. Biomed. Opt. **14**(2), 024016 (2009).
15. S. Hariri, A. A. Moayed, A. Dracopolos, C. Hyun, S. Boyd, and K. Bizheva, "Limiting factors to the OCT axial resolution for in-vivo imaging of human and rodent retina in the 1060 nm wavelength range," Opt. Express **17**(26), 24304–24316 (2009).
16. D. M. de Bruin, D. L. Burnes, J. Loewenstein, Y. Chen, S. Chang, T. C. Chen, D. D. Esmaili, and J. F. de Boer, "In vivo three-dimensional imaging of neovascular age-related macular degeneration using optical frequency domain imaging at 1050 nm," Invest. Ophthalmol. Vis. Sci. **49**(10), 4545–4552 (2008).
17. K. Maaijwee, P. R. Van Den Biesen, T. Missotten, and J. C. Van Meurs, "Angiographic evidence for revascularization of an rpe-choroid graft in patients with age-related macular degeneration," Retina **28**(3), 498–503 (2008).
18. M. G. Cereda, B. Parolini, E. Bellesini, and G. Pertile, "Surgery for CNV and autologous choroidal RPE patch transplantation: exposing the submacular space," Graefes Arch. Clin. Exp. Ophthalmol. **248**(1), 37–47 (2010).
19. B. Považay, B. Hermann, A. Unterhuber, B. Hofer, H. Sattmann, F. Zeiler, J. E. Morgan, C. Falkner-Radler, C. Glittenberg, S. Blinder, and W. Drexler, "Three-dimensional optical coherence tomography at 1050 nm versus 800 nm in retinal pathologies: enhanced performance and choroidal penetration in cataract patients," J. Biomed. Opt. **12**(4), 041211 (2007).
20. R. Leitgeb and M. Wojtkowski, "Complex and Coherence Noise Free Fourier Domain Optical Coherence Tomography," in *Optical Coherence Tomography: Technology and Applications* W. Drexler and J.G. Fujimoto, eds. (Springer, 2008), pp. 190–197.
21. R. K. Manapuram, V. G. R. Manne, and K. V. Larin, "Development of Phase-Stabilized Swept-Source OCT for the Ultrasenstive Quantification of Microbubbles," Laser Phys. **18**(9), 1080–1086 (2008).
22. B. Vakoc, S. Yun, J. de Boer, G. Tearney, and B. Bouma, "Phase-resolved optical frequency domain imaging," Opt. Express **13**(14), 5483–5493 (2005).
23. D. C. Adler, R. Huber, and J. G. Fujimoto, "Phase-sensitive optical coherence tomography at up to 370,000 lines per second using buffered Fourier domain mode-locked lasers," Opt. Lett. **32**(6), 626–628 (2007).
24. J. Zhang and Z. Chen, "In vivo blood flow imaging by a swept laser source based Fourier domain optical Doppler tomography," Opt. Express **13**(19), 7449–7457 (2005).
25. Y. Zhao, Z. Chen, C. Saxer, S. Xiang, J. F. de Boer, and J. S. Nelson, "Phase-resolved optical coherence tomography and optical Doppler tomography for imaging blood flow in human skin with fast scanning speed and high velocity sensitivity," Opt. Lett. **25**(2), 114–116 (2000).
26. B. White, M. Pierce, N. Nassif, B. Cense, B. Park, G. Tearney, B. Bouma, T. Chen, and J. de Boer, "In vivo dynamic human retinal blood flow imaging using ultra-high-speed spectral domain optical coherence tomography," Opt. Express **11**(25), 3490–3497 (2003).
27. Y. Zhao, Z. Chen, C. Saxer, Q. Shen, S. Xiang, J. F. de Boer, and J. S. Nelson, "Doppler standard deviation imaging for clinical monitoring of in vivo human skin blood flow," Opt. Lett. **25**(18), 1358–1360 (2000).
28. R. K. Wang and S. Hurst, "Mapping of cerebro-vascular blood perfusion in mice with skin and skull intact by Optical Micro-AngioGraphy at 1.3 mum wavelength," Opt. Express **15**(18), 11402–11412 (2007).
29. M. Szkulmowski, A. Szkulmowska, T. Bajraszewski, A. Kowalczyk, and M. Wojtkowski, "Flow velocity estimation using joint Spectral and Time domain Optical Coherence Tomography," Opt. Express **16**(9), 6008–6025 (2008).
30. H. C. Hendargo, R. P. McNabb, A. H. Dhalla, N. Shepherd, and J. A. Izatt, "Doppler velocity detection limitations in spectrometer-based versus swept-source optical coherence tomography," Biomed. Opt. Express **2**(8), 2175–2188 (2011).
31. B. Baumann, B. Potsaid, M. F. Kraus, J. J. Liu, D. Huang, J. Hornegger, A. E. Cable, J. S. Duker, and J. G. Fujimoto, "Total retinal blood flow measurement with ultrahigh speed swept source/Fourier domain OCT," Biomed. Opt. Express **2**(6), 1539–1552 (2011).
32. B. Potsaid, B. Baumann, D. Huang, S. Barry, A. E. Cable, J. S. Schuman, J. S. Duker, and J. G. Fujimoto, "Ultrahigh speed 1050nm swept source/Fourier domain OCT retinal and anterior segment imaging at 100,000 to 400,000 axial scans per second," Opt. Express **18**(19), 20029–20048 (2010).
33. B. J. Vakoc, S. H. Yun, G. J. Tearney, and B. E. Bouma, "Elimination of depth degeneracy in optical frequency-domain imaging through polarization-based optical demodulation," Opt. Lett. **31**(3), 362–364 (2006).
34. J. Xi, L. Huo, J. Li, and X. Li, "Generic real-time uniform K-space sampling method for high-speed swept-source optical coherence tomography," Opt. Express **18**(9), 9511–9517 (2010).
35. A. C. Akcay, J. P. Rolland, and J. M. Eichenholz, "Spectral shaping to improve the point spread function in optical coherence tomography," Opt. Lett. **28**(20), 1921–1923 (2003).
36. C. Dorrer, N. Belabas, J. Likforman, and M. Joffre, "Spectral resolution and sampling issues in Fourier-transform spectral interferometry," J. Opt. Soc. Am. B **17**(10), 1795–1802 (2000).

#150555 - $15.00 USD Received 5 Jul 2011; revised 10 Sep 2011; accepted 17 Sep 2011; published 5 Oct 2011

37. B. Cense, N. Nassif, T. Chen, M. Pierce, S. H. Yun, B. Park, B. Bouma, G. Tearney, and J. de Boer, "Ultrahigh-resolution high-speed retinal imaging using spectral-domain optical coherence tomography," Opt. Express **12**(11), 2435–2447 (2004).
38. M. Wojtkowski, V. Srinivasan, T. Ko, J. Fujimoto, A. Kowalczyk, and J. Duker, "Ultrahigh-resolution, high-speed, Fourier domain optical coherence tomography and methods for dispersion compensation," Opt. Express **12**(11), 2404–2422 (2004).
39. N. V. Iftimia, D. X. Hammer, C. E. Bigelow, D. I. Rosen, T. Ustun, A. A. Ferrante, D. Vu, and R. D. Ferguson, "Toward noninvasive measurement of blood hematocrit using spectral domain low coherence interferometry and retinal tracking," Opt. Express **14**(8), 3377–3388 (2006).
40. R. Tripathi, N. Nassif, J. S. Nelson, B. H. Park, and J. F. de Boer, "Spectral shaping for non-Gaussian source spectra in optical coherence tomography," Opt. Lett. **27**(6), 406–408 (2002).
41. Y. Yasuno, V. D. Madjarova, S. Makita, M. Akiba, A. Morosawa, C. Chong, T. Sakai, K. P. Chan, M. Itoh, and T. Yatagai, "Three-dimensional and high-speed swept-source optical coherence tomography for in vivo investigation of human anterior eye segments," Opt. Express **13**(26), 10652–10664 (2005).
42. M. Gora, K. Karnowski, M. Szkulmowski, B. J. Kaluzny, R. Huber, A. Kowalczyk, and M. Wojtkowski, "Ultra high-speed swept source OCT imaging of the anterior segment of human eye at 200 kHz with adjustable imaging range," Opt. Express **17**(17), 14880–14894 (2009).
43. Y. Chen, D. M. de Bruin, C. Kerbage, and J. F. de Boer, "Spectrally balanced detection for optical frequency domain imaging," Opt. Express **15**(25), 16390–16399 (2007).
44. B. D. Goldberg, B. J. Vakoc, W. Y. Oh, M. J. Suter, S. Waxman, M. I. Freilich, B. E. Bouma, and G. J. Tearney, "Performance of reduced bit-depth acquisition for optical frequency domain imaging," Opt. Express **17**(19), 16957–16968 (2009).
45. T. Klein, W. Wieser, C. M. Eigenwillig, B. R. Biedermann, and R. Huber, "Megahertz OCT for ultrawide-field retinal imaging with a 1050 nm Fourier domain mode-locked laser," Opt. Express **19**(4), 3044–3062 (2011).
46. N. Nassif, B. Cense, B. H. Park, S. H. Yun, T. C. Chen, B. E. Bouma, G. J. Tearney, and J. F. de Boer, "In vivo human retinal imaging by ultrahigh-speed spectral domain optical coherence tomography," Opt. Lett. **29**(5), 480–482 (2004).
47. B. Park, M. C. Pierce, B. Cense, S. H. Yun, M. Mujat, G. Tearney, B. Bouma, and J. de Boer, "Real-time fiber-based multi-functional spectral-domain optical coherence tomography at 1.3 microm," Opt. Express **13**(11), 3931–3944 (2005).
48. T. Schmoll, C. Kolbitsch, and R. A. Leitgeb, "Ultra-high-speed volumetric tomography of human retinal blood flow," Opt. Express **17**(5), 4166–4176 (2009).
49. S. Yoneya and M. O. Tso, "Angioarchitecture of the human choroid," Arch. Ophthalmol. **105**(5), 681–687 (1987).

1. Introduction

Optical Coherence Tomography (OCT) is an optical interferometric imaging technique analogous to ultrasound and has its main applications in tissue structure imaging [1]. Due to its non-invasive character and high axial resolution (2-15 μm) this technique has been quickly adopted by the clinical community in fields such as ophthalmology, dermatology and cardiology for the characterization of tissue pathology. The introduction of Fourier-Domain OCT (FD-OCT) technology has played an important role in the increasing popularity of OCT due to its improved detection sensitivity and acquisition speed compared to Time-Domain OCT technology [2–4]. These advantages make it possible to obtain high quality video rate imaging of in vivo tissue structures with reduced motion artifacts [5].

In OCT tissue depth-profiles are measured from interference fringes that are formed when reflected light from a sample interferes with a reference beam. The FD-OCT form uses spectral detection to measure interference fringes as a function of wavenumber, which can be realized by two different hardware implementations. Spectral-Domain OCT (SD-OCT) uses a broadband light source and a spectrometer for detection [6] while Optical Frequency Domain Imaging (OFDI), also known as Swept-Source OCT, uses a rapidly wavelength tuned narrow-band laser and a (balanced) photo-detector [7,8]. The absence of moving parts in SD-OCT makes it superior in terms of optical alignment stability and the exact reproduction of wavenumber sampling in subsequently measured interference fringes. In OFDI the mechanical wavelength tuning creates small variations in wavelength sweeps, trigger timing and sampling which adversely affects the reproducibility of interference fringes. Although this gives potential difficulties with phase-resolved detection and fixed-pattern noise removal, OFDI has an advantage over SD-OCT since it is less sensitive to fringe washout [9,10] and has a lower signal decay with depth [8]. OFDI is therefore rapidly becoming the dominant FD-OCT form in experimental research, especially outside ophthalmology where the tissue of interest is usually several millimeters thick.

#150555 - $15.00 USD Received 5 Jul 2011; revised 10 Sep 2011; accepted 17 Sep 2011; published 5 Oct 2011

In ophthalmology OCT is nowadays widely used for the detection and monitoring of ocular abnormalities in both the anterior and posterior segments of the eye. The outer boundary of the eye (the anterior segment) is easily accessible for OCT measurements and is minimally affected by light absorption due to the aqueous ocular content. This is in stark contrast to the posterior segment for which about 24 mm of aqueous content has to be traversed during which the OCT light is attenuated by water absorption. Light sources in the 850 nm wavelength region have therefore become popular for retinal OCT imaging since this wavelength range is minimally absorbed by water and potentially provides ultra-high axial resolution in the order of a few micrometers [11]. The depth penetration in tissue of 850 nm light is however limited by tissue scattering which especially limits the visualization of structures below the retinal pigment epithelium (RPE). Recently it has been shown that light sources in the 1050 nm region show better penetration in the deeper retinal layers due to lower scattering [12–14] at the expense of a slightly reduced axial resolution [15]. The deep penetration of 1050 nm light allows imaging of the choroidal blood vessel network. This is of particular interest in the detection and evaluation of ocular diseases such as wet age-related macular degeneration in which blood vessels grow from the choroid into the retina [16]. Further, it gives the possibility to evaluate surgical procedures that have their impact below the retina, like transplantations of the RPE and the choroid [17,18], and it improves the imaging in patients with cataract [19].

In OCT the image quality can be severely degraded by fixed-pattern noise [20]. This type of artifact manifests as horizontal lines across the image and originates from unintended reflections within the interferometer, the sample arm optics or the light source. Unlike the interference fringes created by sample reflections fixed-pattern noise creates modulations with a fixed frequency, amplitude and phase in subsequent A-lines. It has been shown for SD-OCT that this property can be used to remove fixed-pattern noise from raw A-line spectra by subtraction of a fringe that only contains fixed-pattern noise information [5,20]. The magnitude of artifact suppression achieved by this method is highly dependent on the reproducibility of the wavenumber sampling of the fringes. This method is therefore less suitable for OFDI since this technique has a lower reproducibility performance, i.e. a lower phase-stability, than SD-OCT. In order to remove fixed-pattern noise in OFDI in a similar way the phase-stability of OFDI has to be improved.

The phase-stability of OFDI systems has been investigated for the purpose of (blood) flow measurements with phase-resolved OCT [21–24]. In this technique (blood) flow is detected from phase-shifts between successive A-lines caused by the Doppler effect. Various implementations of this technique have been reported including phase difference [25,26], phase variance [27], optical micro-angiography [28] and joint spectral-time domain [29] methods. In the majority of these methods it is necessary that the wavenumber sampling of successive A-lines is the same in order to keep the measurement of phase-shifts free from error. In a previous implementation of phase-resolved OFDI this requirement was met by the use of highly accurate triggering hardware [21,30]. An alternative solution was found in the correction of the measured phase during post-processing [22–24,31]. These methods were however focused on the imaging of (blood) flow only and are either not suitable or never shown for the purpose of fixed-pattern noise removal.

In this paper we present a phase-resolved OFDI system at 1 μm to combine low signal decay in depth with high tissue penetration for the evaluation of choroidal blood flow in the human eye. A new post-processing approach is described to obtain phase-stable interference fringes that permit suppression of fixed-pattern noise up to 39.0 dB, which effectively removes these artifacts from the OCT-images. Further we show a system noise performance less than 1 dB from the theoretical shot-noise with a sensitivity of 99.1 dB. Using this system we show in-vivo phase-resolved blood flow imaging in a healthy volunteer and a patient after a RPE and choroid transplantation procedure.

#150555 - $15.00 USD Received 5 Jul 2011; revised 10 Sep 2011; accepted 17 Sep 2011; published 5 Oct 2011

2. Experimental system description

2.1 Light source

The developed OFDI system uses a high-speed short-cavity swept-source laser (Axsun Technologies Inc, MA, USA) in the 1 µm wavelength range similar as reported by Potsaid *et al.* [32]. The light-source has a center wavelength of 1040 nm and a usable bandwidth of 106 nm. The axial resolution was measured to be 6.5 µm in air (4.7 µm in tissue, n_{tissue}=1.38). Unidirectional wavelength sweeping (short to long wavelengths) occurs at a repetition of 100 kHz with a duty cycle of nearly 50%. During the dead time the laser gain element is turned off to prevent wavelength scanning in the opposite direction when the tunable wavelength filter of the source scans back to its initial position. The time-averaged optical power was 13.5 mW. An electronic sweep-trigger is supplied by the laser to trigger the acquisition of individual A-lines. Additionally a non-linear optically derived data sampling clock is provided to acquire laser sweeps linear in wavenumber space. In the current study this last option was not used.

2.2 Interferometer

Light emitted by the swept-source laser was coupled into a fiber-based interferometer (Fig. 1) where it was split into a sample arm and a reference arm by a 20/80 fiber-coupler. The sample-arm light was directed to galvanometer based XY-scanning optics in an ocular slit lamp to image the posterior segment of the human eye. The light leaving the slit lamp had a bundle diameter of 2.2 mm and a power of 1.7 mW. A 10/90 fiber coupler directed 90% of the reference arm light through an air gap to match the optical chromatic dispersion of the sample arm optics. A diaphragm was placed in this air gap to control the amount of reference arm light in the detection. The sample and reference arms were recombined by a 50/50 fiber-coupler for dual-balanced detection of the interference signals by a balanced photo-receiver (PDC-130 350MHz, Thorlabs, NJ, USA). A 10% tap of the reference arm light was coupled into a Mach-Zehnder Interferometer (MZI) which created a stable interference fringe to measure the non-linear wavenumber sampling and to phase-stabilize each laser sweep. In the MZI the light was split into two arms using a 70/30 fiber coupler each passing the light through an air-gap before the light was detected with a 50/50 fiber coupler on a balanced photo-receiver (Thorlabs PDC-130). The air gaps of the MZI were mismatched by 2.2 mm to create a 47 MHz signal.

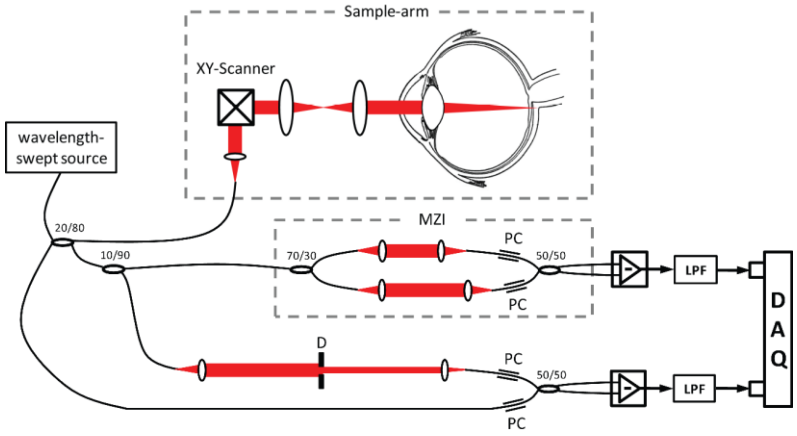

Fig. 1. Schematic drawing of the OFDI setup. D: diaphragm; DAQ: data-acquisition system; LPF: low-pass filter; MZI: Mach-Zehnder Interferometer; PC: in-line polarization controller.

2.3 Data-acquisition

After detection the signals from both interferometers were filtered to reduce high-frequency noise using low-pass filters (filter-types BLP200+ & BLP150+ for imaging interferometer

#150555 - $15.00 USD Received 5 Jul 2011; revised 10 Sep 2011; accepted 17 Sep 2011; published 5 Oct 2011

and MZI respectively; Mini-circuits, NY, USA) and recorded by a 14-bit resolution dual-channel data-acquisition (DAQ) board (PX14400, Signatec Inc., CA, USA) at a 400 MHz sampling rate. The data-acquisition was synchronized with the analog signal generation board (NI PCIe-6353, National Instruments, TX, USA) which drove the XY-scanning optics in the slit lamp. The acquired data was stored and a portion was processed for real-time display using custom-made software written in LabVIEW (National Instruments, TX, USA) and C ++ . Each digitized wavelength-sweep consisted of 1860 samples (200 pre-trigger samples).

3. Digital signal processing

In order to obtain Fourier-transform limited axial resolution, optimal sensitivity performance and artifact free (phase-resolved) imaging in OFDI it is necessary to correct acquired interference fringes for several factors including non-linear wavenumber spacing, optical chromatic dispersion, fixed-pattern noise and coherence function sidelobes. These corrections can be implemented in hardware by the use of non-linear sample clocks [33,34], dispersion compensation prisms and water cells, highly accurate balanced detection, and hardware optical spectral shaping respectively [35]. A significant reduction in post-acquisition signal processing can be achieved with these solutions at the expense of increased complexity and demands on hardware accuracy. Equivalent software post-processing approaches like signal resampling [8,36], numerical dispersion compensation [37–39], fixed-pattern noise subtraction [5] and numerical spectral shaping [40] are therefore still widely used.

In the post-processing algorithm presented in this paper phase-stabilization for acquired interference fringes is achieved *prior to* signal resampling and other correction steps by analysis of the MZI measured wavenumber sampling of each interference fringe.

3.1 Phase-stabilization algorithm

Instabilities in the swept-source laser, the interferometer, and the data-acquisition hardware result in a different (non-linear) wavenumber sampling and a shift in the digitized wavenumber range (k-space) for subsequent A-lines. In order to obtain phase-stable A-lines a signal resampling procedure is needed that corrects both effects.

In the presented OFDI system the wavenumber sampling of individual A-lines was measured from simultaneously recorded MZI signals. An exaggerated example is shown in Fig. 2A for two A-lines and their MZI signals. The k-space for each A-line is visualized in a color bar which shows a wavenumber shift (different starting color) and a different wavenumber sampling (different non-linear color distribution) for the two A-lines. The wavenumber sampling was measured from the MZI signals by a phase oriented analysis using Hilbert transformation as described earlier [41,42] which gives the local (instantaneous) phase angle of each individual MZI signal sample. After unwrapping for 2π phase-jumps the resulting phase-curves, plotted in Fig. 2B, can be used to correct differences in wavenumber sampling and to linearize both A-lines. This is visualized in Fig. 2C in which the MZI signals are plotted as a function of their unwrapped phase angles, resulting in linear MZI signals with perfect wave cycle alignment. However, a shift in the digitized wavenumber range larger than a single wave cycle causes a misalignment in k-space of 2π or multiples thereof, visualized as a shift in the colorbar between the two MZI signals in Fig. 2C. This problem is a direct consequence of the phase unwrapping algorithm that corrects 2π phase-jumps with respect to the phase angle of the first data sample. Cross-correlation was used to measure the shift magnitude in 2π increments between the two MZI signals and the resulting shift was used to correct the unwrapped phase-curve of the second MZI signal. This is shown in Fig. 2D where the red phase curve is shifted down compared to Fig. 2B. Before cross-correlation the MZI signals were resampled to a linear k-space to avoid problems with differences in wavenumber sampling. The corrected MZI phase-curves can now be used to exactly align, and therefore phase-stabilize, the two A-lines. This is shown in Fig. 2E where the two A-lines and their MZI signals are plotted as a function of the corrected unwrapped MZI phase. After the phase-stabilization procedure each individual A-line was resampled to the same linearly spaced phase-trace to obtain phase-stabilized A-lines linear in k-space.

#150555 - $15.00 USD Received 5 Jul 2011; revised 10 Sep 2011; accepted 17 Sep 2011; published 5 Oct 2011

Phase-stabilization of large sets of A-lines can be achieved by the use of a reference MZI signal with respect to which all other A-lines are stabilized. The reference MZI signal can in principle be taken from the currently processed set of A-lines or taken from an earlier measurement if phase-stabilization in between data sets is necessary.

In case the optical path length or the amount of optical chromatic dispersion of the MZI is different from the imaging interferometer it is necessary to correct the MZI phase-curves before A-line resampling. This correction can easily be determined from the differences in the local phase of the MZI and a simultaneously measured mirror reflection in the imaging interferometer.

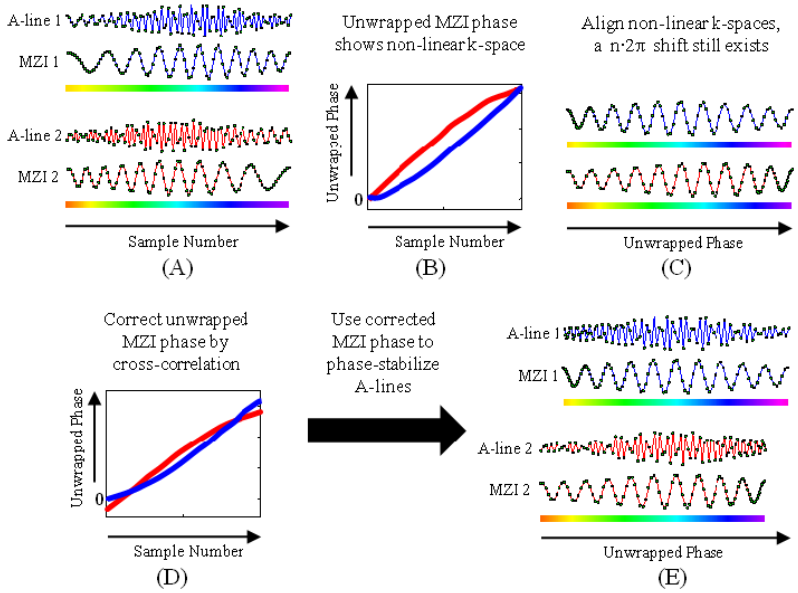

Fig. 2. Schematic representation of the phase-stabilization algorithm. (A) Two A-lines and their MZI signals plotted as a function of sample number. Different non-linear wavenumber sampling and shifts are observed. The colorbar shows the wavenumber distribution. (B) The unwrapped local phase of the MZI signals as a function of sample number shows the non-linear wavenumber sampling. (C) The MZI signals plotted as a function of the unwrapped local phase which shows k-space linearization and aligned wave-cycles, but a shift is still present. (D) Unwrapped phase curves as a function of sample number after correction for shifts as measured by cross-correlation (red curve shifted down compared to (B)). (E) The A-lines of (A) plotted as a function of the corrected unwrapped phase, which shows phase-stabilization between the A-lines.

3.2 Implementation of post-processing algorithms

Recorded retinal data was first phase-stabilized and resampled to a linear k-space as described above. Fixed-pattern noise was removed by subtracting the average spectrum from each individual A-line spectrum [5]. Since the fixed-pattern noise showed a small drift in its phase over time the average A-line spectrum was computed from 8400 successively recorded A-lines using a moving average. The side-lobes of the coherence function were minimized by apodization with a tapered cosine window. Finally, optical chromatic dispersion was numerically compensated by optimizing the variance of the A-lines [39]. OFDI intensity images were obtained from magnitude data after Fourier-transformation of the processed retinal data. The corresponding phase information was used to obtain bi-directional flow images by calculation of the phase-difference in adjacent A-lines [25,26]. Phase-wrapping and bulk-motion were corrected as described by White *et al.* [26].

#150555 - $15.00 USD Received 5 Jul 2011; revised 10 Sep 2011; accepted 17 Sep 2011; published 5 Oct 2011

3.3 Advantages and disadvantages of the proposed phase-stabilization method

In a recent study by Hendargo *et al.* [30] phase-stabilization for an OFDI system with the same swept-laser source was obtained by using the laser's optically derived sampling clock in combination with a highly accurate A-line trigger signal derived from a fiber-bragg grating. The advantage of this approach over the current method is the reduced amount of post-processing that is necessary after the acquisition. In the current method the average time to process a 3D-data set of 250 B-scans with 2000 A-lines/B-scan was 21 minutes on a computer system equipped with an Intel Xeon X5550 quad core processor @ 2.67 GHz and 12 GB of RAM. Although no post-processing time was published by Hendargo, we expect it to be considerably less. Further, in the current approach two data-channels were used simultaneously instead of a single data-channel as for Hendargo's case. The usage of the second data-channel put higher demands on storage capacity with a size of ~4.0 GB for each raw 3D-data set. This data set size can be brought back to half its original size when using a single data-channel and is potentially further reduced by a more efficient sampling with optical clocking [34]. The same comparisons can be made to a lesser extent for a study published by Baumann *et al.* [31] in which phase-stabilization was obtained from a glass plate embedded in the sample-arm. Although a single data-channel was used in this study the post-processing time should be longer than Hendargo *et al.* since numerical resampling was used instead of optical clocking. Further the method of Baumann *et al.* does not align the recorded spectra to such an extent that all fixed-pattern noise could be subtracted.

The advantage of the proposed phase-stabilization method in this study is that it can provide phase-stable data for systems with less complex hardware without optical clocking and optical triggering. The method is highly flexible since the user has full-control over all processing steps and is less restricted by hardware limitations. The accuracy of phase-stabilization is for instance easy to set by the user since it mainly depends on the signal-to-noise ratio of the MZI (see section 4.2). This results in the ability to measure phase-shifts at a noise-level down to the theoretical limit (see section 4.2), to completely remove fixed-pattern noise and to obtain artifact free (phase-resolved) images (see section 5).

4. Technical performance

4.1 Signal-to-noise ratio and sensitivity analysis

The signal-to-noise ratio (SNR) of OCT systems is highly dependent on the amount of power used in the reference arm of the interferometer and is ideally adjusted to a level where the shot-noise dominates all other noise sources. In this case the noise power of the OCT-system is primarily due to the quantized detection of photons and increases linearly with the reference arm power. In order to achieve a SNR as close to the shot-noise as possible a systematic analysis of the different noise sources in the developed OFDI-system was performed and the optimal reference arm power was selected. The analysis was done according to a method described earlier [43,44] in which the noise in an OFDI-system was separated in four uncorrelated noise sources: thermal noise (detector noise), shot-noise, relative intensity noise (RIN) and DAQ-noise. Quantization noise due to the bit-resolution of the acquisition was left out of the current analysis since it was shown that the contribution of this noise source was negligible at a 14-bits acquisition resolution [44]. In order to determine the optimal SNR the reference arm power was varied by adjusting the diaphragm in the air gap and the absolute noise power was evaluated at the detector [43]. During this analysis the reference arm powers were measured using the optical power monitor outputs of the balanced receiver and the sample arm was blocked. The noise spectra were calculated by averaging 1000 Fourier-transformed A-lines that were phase-stabilized, resampled to linear k-space and from which fixed-pattern noise was removed. The noise power of individual noise sources were determined by sequentially adding extra noise sources to the measurements in the following order: DAQ-noise, thermal noise, and RIN + shot-noise. To obtain the true noise power of a single noise source the spectra of the preceding noise sources were subtracted. Since RIN cannot be measured without the contribution of shot-noise, the theoretical (calculated) shot-

#150555 - $15.00 USD Received 5 Jul 2011; revised 10 Sep 2011; accepted 17 Sep 2011; published 5 Oct 2011

noise was subtracted to determine the RIN power. The RIN was determined under unbalanced detection conditions only since it was strongly dominated by the other noise sources under balanced detection conditions. Finally, also the total noise under balanced detection conditions was measured for comparison with the theoretical shot-noise.

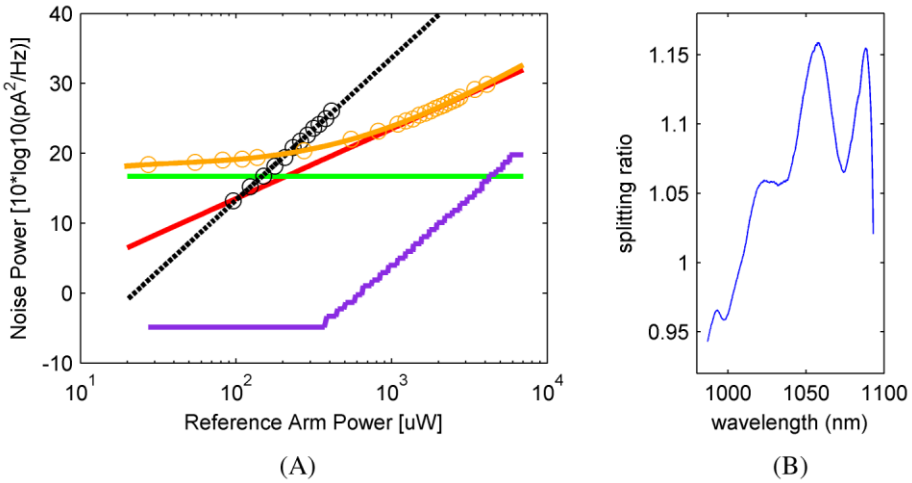

Fig. 3. (A) Characterization of the system noise as a function of the reference arm power at a carrier frequency of 100 MHz. The total noise (orange) is decomposed in the four primary noise components: DAQ noise (violet), thermal noise (green), unbalanced RIN (black) and theoretical shot-noise (red). The noise power is expressed as noise current squared in decibel at the detector. Circles represent experimental data; lines are fits to experimental data. Optimal SNR performance was found for a reference arm power of 1.5 mW. (B) The spectrally depended splitting ratio of the 50/50 fiber coupler used in the balanced detection.

An example of the contribution of each noise term with increasing reference arm power is shown in Fig. 3A for a carrier frequency of 100 MHz. The DAQ-noise is visualized in violet as a step function due to the increasing vertical acquisition range that is needed when measuring at higher optical powers. The thermal-noise is displayed as a green horizontal line since it is independent of reference arm power. The theoretical shot-noise is given by the red linearly increasing line. The black circles give measured unbalanced RIN power and a linear fit is plotted as a black dashed line as a guide to the eye. The total noise of the system is displayed as orange circles with a polynomial line fit. Figure 3A clearly shows a range of reference arm powers from 1mW to 4 mW for which the shot-noise is the most dominant noise source and is almost equivalent to the total noise. Shot-noise limited SNR can only be achieved when the contribution of balanced RIN to the total noise is minimal and its noise power is significantly lower than the shot-noise. The RIN suppression by balanced detection was therefore at least 20 dB and reduced the RIN to a level that was at least 6 dB below the shot-noise. In order to choose the optimal reference arm power over the full measurement bandwidth (DC - 200 MHz) this analysis was done for different carrier frequencies. The difference between the total noise and the theoretical shot-noise was calculated and it was observed that for carrier frequencies below 170 MHz the difference between the measured total noise and the theoretical shot-noise was smaller or equal to 1 dB in a reference arm power range from 1mW to 2.5 mW. High carrier frequencies above 170 MHz experienced a higher noise power up to a difference of 3 dB with the shot-noise due to aliased thermal noise from frequencies above the Nyquist frequency (200 MHz). A reference arm power of 1.5 mW gave the lowest overall difference between the total noise and the theoretical shot-noise and was selected for further measurements.

In a recent publication of Klein *et al.* [45] it was stated that many 1050 nm OFDI systems operate more than 3 dB away from the shot-noise due to insufficient RIN suppression caused by spectral depended splitting in the balanced detection. A spectral symmetric Michelson

#150555 - $15.00 USD Received 5 Jul 2011; revised 10 Sep 2011; accepted 17 Sep 2011; published 5 Oct 2011

interferometer was proposed to reduce this effect and shot-noise limited performance was obtained. In the current study an interferometer is used with a standard 50/50 fiber coupler (Gould Fiber Optics). The spectral deviation between the two fiber leads at the detector was measured to be 16% at most (Fig. 3B). Performance close to the shot-noise limit is however still possible due to the low RIN of the Axsun swept-source laser. The RIN was calculated as described by Chen *et al.* [43] according to RIN = N_{RIN} $(h\nu / \eta q P_{ref})^2$ with N_{RIN} as the unbalanced RIN noise power [A^2/Hz] as given in Fig. 3A, P_{ref} as the corresponding optical reference arm power, h as Planck's constant, ν as the optical frequency, η as the quantum efficiency of the detector, and q as the elementary charge. A RIN of −142.2 dB/Hz was calculated which is substantially (16.8 dB to 31.2 dB) lower than other published results on 1050 nm swept-source lasers as for instance by Chen *et al.* who reported −111 dB/Hz for a 30 kHz A-line repetition [43] and Klein *et al.* who reported −125.4 dB/Hz and −121.9 dB/Hz for 684 kHz and 1.37 MHz repetition rates respectively (mean RIN percentages of 1% and 1.5% for a 350 MHz bandwidth) [45]. For our swept-source laser the RIN suppression by balanced detection with a standard 50/50 fiber coupler is therefore enough to get system performance very close to the shot-noise limit.

In OFDI the sensitivity depends on depth due to the finite instantaneous linewidth of the swept-source laser. The maximum obtainable sensitivity was measured from a reflection of a mirror that was placed in front of the slit-lamp close to the zero-delay point. A neutral density filter (Thorlabs NDUV30A, OD 3.0) was inserted in between to prevent signal saturation and provided a single-pass attenuation of 25.3 dB at 1050 nm. The sensitivity was obtained from 1000 successively measured A-line spectra that were zeropadded to 4096 samples and Fourier-transformed. Subsequently, the power spectral density (PSD) ($Re^2 + Im^2$) of each A-line was calculated. The average PSD over all A-lines was calculated and the sensitivity was measured from the average PSD as the ratio between the mirror reflection peak and the mean noise-floor as described by Nassif *et al.* [46]. Finally, 50.6 dB was added to compensate the double-pass attenuation of the neutral density filter. A sensitivity of 99.1 dB was measured at a depth of 0.283 mm, which differed from the theoretical sensitivity of 108 dB due to optical losses in the 80/20 fiber coupler and in the slit-lamp and a 4 dB loss due to inefficient coupling through the ophthalmic lens on the mirror. The sensitivity decay with depth was measured on a mirror in a dummy sample-arm and fell off with 6 dB over a depth displacement of 4.2 mm. The measured maximum sensitivity and sensitivity decay with depth are similar as earlier reported for this swept-source laser by Potsaid *et al.* [32].

4.2 Phase-stability analysis

The accuracy of phase-resolved measurements and the removal of fixed-pattern noise both depend on the phase-stability performance of the OFDI system. Phase-stability can be measured by analyzing the phase-difference between successive A-lines as measured on a stationary mirror [26]. The phase-difference values follow a Gaussian probability distribution in which the standard deviation $\sigma_{\Delta\phi}$ describes the phase-noise. When our OFDI system is phase-stable $\sigma_{\Delta\phi}$ depends only on the SNR and the depth of both the sample and the calibration (MZI) signal as described by Vakoc *et al.* [22]

$$\sigma_{\Delta\phi} = \sqrt{\left(\frac{1}{SNR_s}\right) + \left(\frac{Z_s}{Z_c}\right)^2 \left(\frac{1}{SNR_c}\right)}, \qquad (1)$$

in which SNR_s is the SNR of the sample signal at depth Z_s and SNR_c is the SNR of the calibration signal at depth Z_c.

The phase-stability performance was examined by measuring a stationary mirror at different depths. At each depth 10,000 subsequent A-lines were taken, which were split into 10 data sets of 1000 A-lines. The phase-noise $\sigma_{\Delta\phi}$ of each data set was calculated by taking the standard deviation of the phase-difference values and the mean ± the standard deviation over $\sigma_{\Delta\phi}$ from all 10 data sets was plotted in Fig. 4. The effect of the phase-stabilization algorithm

#150555 - $15.00 USD Received 5 Jul 2011; revised 10 Sep 2011; accepted 17 Sep 2011; published 5 Oct 2011

was investigated by comparison with the same data that was processed without phase-stabilization. This unstabilized data was obtained by linearizing the k-space of each A-line directly using its MZI signal without correcting any shifts between the A-lines. In order to determine if the system was free from additional phase-noise sources, $\sigma_{\Delta\phi}$ is plotted against depth and compared to phase-noise as calculated by (1) using the known values for SNR_s, SNR_c, Z_s, and Z_c at each depth. During the measurements SNR_c and Z_c had fixed values of 59 dB and 1.1 mm respectively, and SNR_s varied along Z_s with a Gaussian sensitivity roll-off starting at 48.1 dB at the zero-delay point to 42.1 dB at 4.2 mm depth.

In Fig. 4A the measured values for $\sigma_{\Delta\phi}$ are plotted against depth as blue dots for the case with phase-stabilization and as red crosses for the case without. The measured standard deviations of these measurements are displayed as vertical error-bars. It is directly evident from this figure that the phase-noise is considerably lower when phase-stabilization is used. This is especially the case at greater depths where the phase-noise without phase-stabilization increases up to a level equal to 38 times the phase-noise under phase-stabilized conditions. In Fig. 4B the phase-noise measured with phase-stabilization is plotted together with the theoretical phase-noise based on Eq. (1) as a green line. It can be seen that the measured phase-noise closely follows the theory indicating the absence of additional phase-noise sources. The small deviations observed from the theoretical line are attributed to reductions in SNR_s due to non-perfect mirror alignment and to mechanical vibrations of the sample-arm mirror. The latter is also responsible for sudden increases in the measured standard deviation of $\sigma_{\Delta\phi}$. A mean $\sigma_{\Delta\phi}$ phase-noise value of 3.9 mrad is measured at a depth of 0.235 mm for a SNR_s of 48.1 dB which corresponds to the theoretical limit. This is better than the previous reported phase-noise performance for a SD-OCT system by Hendargo *et al.* (4 mrad for 53 dB SNR) [30] and considerably better than published results for OFDI systems with the same swept-source laser by Hendargo *et al.* (7 mrad for a 64 dB SNR) [30] and Baumann *et al.* (97 mrad at 100 kHz and 47 mrad at 200 kHz for a 35 dB SNR) [31].

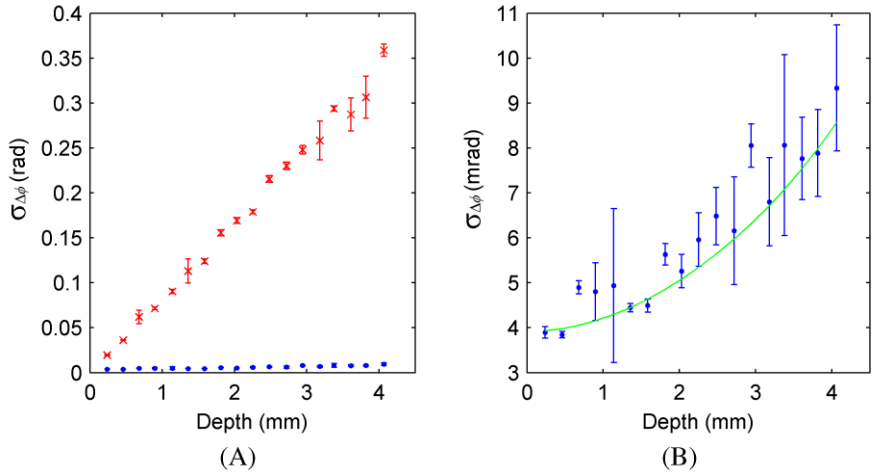

Fig. 4. (A) The phase-noise with (blue dots) and without (red crosses) phase-stabilization is plotted against depth. The standard deviation in these measurements are displayed as error-bars. The phase-noise is significantly lower when phase-stabilization is used, especially at greater depths. (B) The phase-noise measured with phase-stabilization is plotted together with the theoretical phase-noise that is based on Eq. (1) with a SNR_s of 48.1 dB at DC and a Gaussian roll-off of 6 dB over 4.2 mm. A good overall agreement between the measured and calculated phase-noise demonstrates that Eq. (1) is valid and that no other phase-noise sources were present.

The results from the phase-stability analysis indicated that the OFDI system operated phase-stabilized. In this case the alignment accuracy of A-line spectra depends only on the phase-noise of the calibration signal, which was calculated from Eq. (1) by taking SNR_s equal

#150555 - $15.00 USD Received 5 Jul 2011; revised 10 Sep 2011; accepted 17 Sep 2011; published 5 Oct 2011

to infinity. At a depth of 4.5 mm a calibration phase-noise of 4.6 mrad was calculated which gave an A-line alignment accuracy of $1.5 \cdot 10^{-3}$ samples. This is equivalent to a wavelength assignment accuracy of 87 fm.

4.3 In-vivo flow sensitivity analysis

In-vivo blood-flow is detected by the difference in phase between successive A-lines. This method inherently assumes that both A-lines are obtained from the same location in the sample, which is not true when lateral scanning is used to obtain a B-scan [47]. The difference in measured sample structure causes an additional phase-noise term $\sigma_{\Delta x}$ that is based on random phases at a particular point in the sample and the displacement of the beam compared to its spot size [47]

$$\sigma_{\Delta x} = \sqrt{\frac{4\pi}{3}\left(1-\exp\left(-2\left(\frac{\Delta x}{d}\right)^2\right)\right)}, \qquad (2)$$

in which Δx is the displacement of the spot in between successive A-lines and d is the spot diameter on the retina. Since (1) and (2) are uncorrelated noise sources the total phase-noise σ_{tot} during in-vivo blood-flow measurements can be calculated by quadratic addition

$$\sigma_{tot} = \sqrt{\sigma_{\Delta\phi}^2 + \sigma_{\Delta x}^2}. \qquad (3)$$

In a biological sample the measured phase becomes quickly uncorrelated when scanning laterally and therefore $\sigma_{\Delta x}$ is usually the dominant phase-noise term. In our case a spot displacement Δx of 1.1 µm was used with a spot diameter d of 10 µm. These parameters give a theoretical value for $\sigma_{\Delta x}$ of 0.31 rad.

In order to show the impact of lateral scanning on the phase-noise we first consider the most optimal situation in which the total phase noise is only limited by the SNR_s, hence $\sigma_{tot} = \sqrt{(1/SNR_s)}$. In the case without lateral scanning this situation is approached when the phase-noise due to the sample is bigger than the phase-noise due to the calibration (MZI) signal, which is described by rearranging Eq. (1) to the inequality: $\sqrt{(1/SNR_s)} > \sqrt{((Z_s/Z_c)^2(1/SNR_c))}$. The values for SNR_s for which this inequality is true are indicated in Fig. 5A in which the blue line represents the transition where the phase-noise due to the sample is equal to that from the calibration signal. Samples at a specific depth Z_s that have an SNR_s below the blue line will have a phase-noise that is dominated by the sample itself. Samples at a specific Z_s with a SNR_s above the blue line will have a phase-noise that is dominated by the calibration signal. This figure shows that without lateral scanning sample dominated phase-noise is achieved over the full imaging range for signals with a SNR_s of 45 dB or lower.

In case lateral scanning is used optimal conditions are obtained when the phase-noise due to the sample is bigger than the combined phase-noise of the calibration signal and lateral scanning: $\sqrt{(1/SNR_s)} > \sqrt{((Z_s/Z_c)^2(1/SNR_c) + \sigma^2_{\Delta x})}$. Since $\sigma_{\Delta x}$ changes considerably for different spot displacements multiple transition lines for this situation are plotted in Fig. 5B with *Δx/d* ratios of 0.11 (in black), 0.011 (in green), and 0.0011 (in red) corresponding to spot displacements of 1.1 µm, 0.11 µm and 0.011 µm respectively for a 10 µm spot diameter. Each line indicates the transition where the phase-noise due to the sample is equal to the combined phase-noise of the calibration signal and lateral scanning for its particular *Δx/d* ratio. Figure 5B shows that the smallest plotted *Δx/d* ratio of 0.0011 has a comparable SNR_s range for which the phase-noise due to the sample is dominant as for the case without lateral scanning at a high depth. In practice this *Δx/d* ratio is not used since it demands a very dense A-line sampling of 90,909 A-lines / mm in the lateral direction. A more workable *Δx/d* ratio of 0.11 is therefore used with a sampling of 909 A-lines / mm. Consequently the SNR_s range for which the phase-noise of the sample is dominant decreases to ≤10 dB. This is at least 35 dB lower compared to the case without lateral scanning. In in-vivo measurements SNR_s levels up to around 45 dB are observed. Without lateral scanning this means that SNR_s limited phase-

#150555 - $15.00 USD Received 5 Jul 2011; revised 10 Sep 2011; accepted 17 Sep 2011; published 5 Oct 2011

noise is achieved for practically all measurements, while for the case with lateral scanning the majority of measurements will be dominated by $\sigma_{\Delta x}$.

Equation (3) was verified in in-vivo measurements of the retina of a healthy volunteer. B-scans of 2000 A-lines were taken over a scan width of 2.2 mm at various locations including the macula and optic nerve head regions. Phase-difference information was calculated and retinal areas without blood flow but with significant SNR (≥10 dB) were selected for phase-noise measurement. The phase-noise was calculated by the standard deviation from the phase-difference values in the selected areas. The mean phase-noise as measured over 7 different locations was found to be 0.32±0.03 rad with phase-stabilization and 0.38±0.06 rad without phase-stabilization. Note that the improvement by phase-stabilization will be considerably larger when a smaller spot-displacement Δx is used since $\sigma_{\Delta x}$ is the dominant phase-noise source in this measurement and is not affected by phase-stabilization. During this experiment the retina was located at an average depth of 1.5 mm and had a mean SNR_s of 25 dB. The theoretical total phase-noise calculated for this case is 0.32 rad, which is in good agreement with the experimental result with phase-stabilization. The found in-vivo phase-noise value is comparable to a recently published study with an SD-OCT system by Schmoll *et al.* [48] who reported an in-vivo phase-noise of 0.40 rad for a comparable *Δx/d* ratio. It is also comparable to the 0.37 rad that was reported by Baumann *et al.* [31] who uses an OFDI system with the same swept-source laser as used in this study in a buffered configuration to obtain a sweep repetition rate of 200 kHz. It is however considerably better than the 0.61 rad that Baumann reported for his system running unbuffered at a 100 kHz sweep repetition rate.

The minimum detectable Doppler frequency at a phase-noise level of 0.32 rad is ±5.16 kHz which corresponds to a blood flow velocity of 1.95 mm/s for a 0° angle of incidence between the OCT-beam and the blood flow velocity-vector. Blood flow can be measured free from phase wrapping up to a Doppler frequency of ±50.0 kHz which corresponds to 18.9 mm/s. For a typical angle of 80° during retinal measurements the measurable blood-velocity ranges between 11.2 mm/s and 108.8 mm/s.

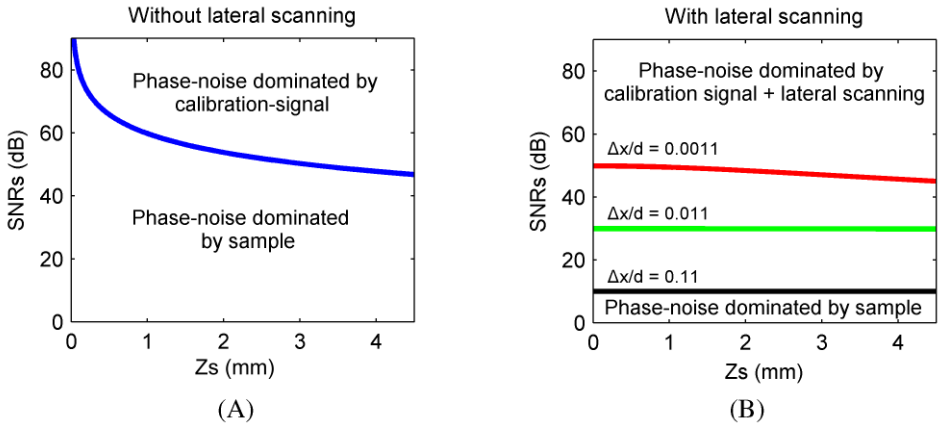

Fig. 5. (A) The phase-noise performance depending on SNR_s and Z_s in case no lateral scanning is used. The blue line indicates the SNR_s level below which the phase-noise is dominated by the sample signal. (B) The phase-noise performance depending on SNR_s and Z_s in case lateral scanning is used. The plotted lines indicates the SNR_s level below which the phase-noise is dominated by the sample signal for *Δx/d* ratios of 0.0011 (red), 0.011 (green), and 0.11 (black). In practice a *Δx/d* ratio of 0.11 is used to get a workable A-line sampling density. Consequently the SNR_s range for which the sample phase-noise is dominant decreases to a level that is at least 35 dB lower than for the case without lateral scanning.

5. Imaging performance

The present study was approved by the local Institutional Review Board and adhered to the tenets of the Declaration of Helsinki. Informed consent was obtained from each subject.

#150555 - $15.00 USD Received 5 Jul 2011; revised 10 Sep 2011; accepted 17 Sep 2011; published 5 Oct 2011

5.1 Fixed-pattern noise removal

In Fig. 6 the effect of fixed-pattern noise removal is shown in an intensity image of the macula of a healthy volunteer. The image has a width of 4.4 mm consisting of 2000 A-lines, a displayed depth of 2.0 mm and a dynamic range of 47.0 dB. When fixed-pattern noise is not subtracted the image quality is degraded at several depths by fixed-pattern noise lines (Fig. 6A). The sources of these artifact lines are remaining non-balanced background signals which are visible above the retina with a maximum SNR of 48.7 dB, and a spectral modulation originating from the swept-source laser that was not totally cancelled by the balanced detection which is visible below the choroid at a depth of 1.52 mm with an SNR of 23.2 dB. In case no phase-stabilization was used these artifact lines were only partly removed by fixed-pattern noise subtraction and were attenuated to respectively 12.1 dB and 13.0 dB (Fig. 6B). The phase-stabilization method permitted to suppress these artifact lines much better. On a mirror the fixed-pattern noise suppression was measured at different depths and showed a reduction of 39.0 dB at the zero-delay point which gradually decreased to 25.5 dB at a depth of 4.0 mm. Except for a thin artifact line at the zero-delay point of 9.7 dB all the fixed-pattern noise lines were removed from the image (Fig. 6C).

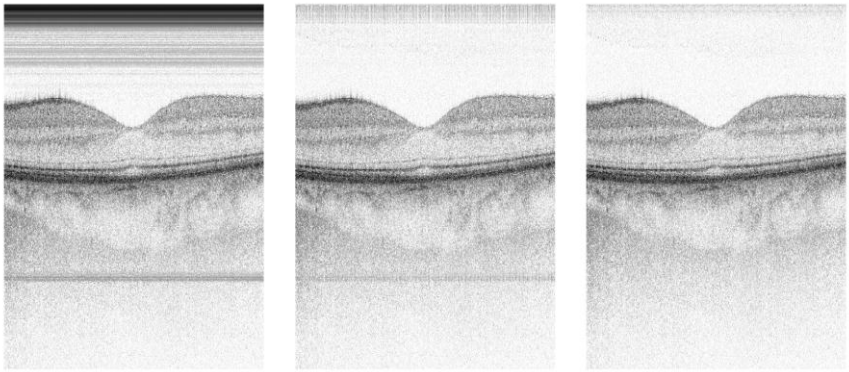

Fig. 6. Fixed-pattern noise removal on an OFDI intensity image of the macula of a healthy volunteer. (A) The image without fixed-pattern noise removal. Artifact lines are clearly visible above the retina and below the choroid; (B) Fixed-pattern noise removal when the phase-stabilization method is not used. The artifact lines are partly removed but still visible. (C) Fixed-pattern noise removal on a phase-stabilized image. The fixed-pattern noise lines are removed except for a thin artifact line at the zero-delay point.

5.2 Phase-noise artifact removal in flow imaging

In Fig. 7 the effect of the phase-stabilization method is shown in flow images of the macula of a healthy volunteer. The corresponding intensity image is shown in Fig. 7A which has a width of 2.2 mm consisting of 2000 A-lines, a displayed depth of 1.36 mm, and a dynamic range of 45.0 dB. The accompanying flow images (Figs. 7B&C) have the same dimensions and are displayed at a dynamic range of 0.3π. In order to objectively assess the improvement by the phase-stabilization algorithm the bulk-motion was left uncorrected. A 2D median filter (3x10 pixels) was used for noise reduction. In Fig. 7B the flow image is shown when the phase-stabilization method was not used, which resulted in vertical phase-artifact lines throughout the imaged tissue, obscuring a clear view on the detected blood-flow. These artifacts were however totally absent when the phase-stabilization method was used as shown in Fig. 7C. Blood-flow is now visible in the choroid region without artifacts.

#150555 - $15.00 USD Received 5 Jul 2011; revised 10 Sep 2011; accepted 17 Sep 2011; published 5 Oct 2011

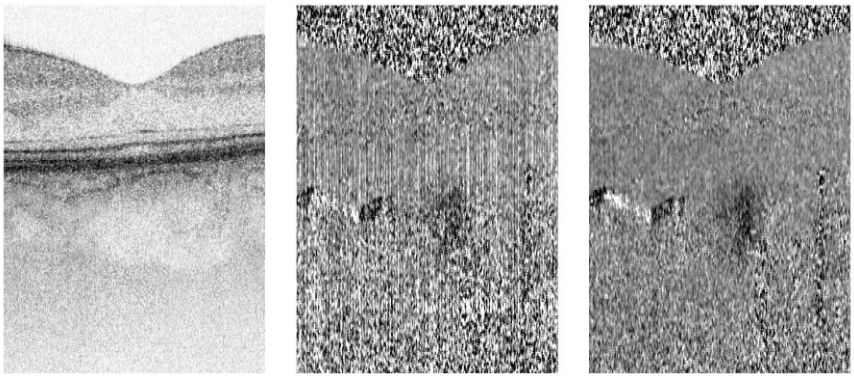

Fig. 7. Phase-noise artifact removal in flow imaging of the macula of a healthy volunteer. (A) The intensity image showing the retinal and choroidal structures. (B) Flow image obtained without phase-stabilization. Vertical phase-artifact lines can be seen throughout the tissue. (C) Flow image obtained with phase-stabilization. The phase-artifact lines are totally absent in this case.

5.3 Flow imaging in a healthy volunteer

The performance of the OFDI system for in-vivo measurement of blood flow is demonstrated by imaging the macula of a healthy volunteer. The retinal surface was scanned over 2.2 mm in width (fast-axis) with 2000 A-lines and over 4.1 mm in height (slow-axis) with 250 B-scans. The data was processed to create cross-sectional intensity (Fig. 8A top) and bi-directional flow (Fig. 8A bottom) images. The bi-directional flow images were filtered for noise by a 2D median filter (3x10 pixels) and a grayscale color coding is used to distinguish areas without flow (gray) from areas with blood flow towards (black) and away (white) from the OCT laser beam. In the examples shown in Fig. 8A blood flow is observed at several locations in the choroid which are indicated by red ellipses. The bi-directional flow image gives complementary information on the vasculature since it reveals blood vessels at positions that are difficult to recognize as such in the intensity image.

The cross-sectional intensity images were manually segmented and the structural information between the retinal nerve fiber layer and the RPE was integrated over depth to create an intensity en-face image of the retinal vasculature (Fig. 8B). This image shows clearly the vasculature in the retina for which blood flow is expected to be measured. A corresponding en-face image of the retinal flow was obtained by integration over the absolute values of the bi-directional flow images for the segmented areas (Fig. 8C). In the calculation of this image the phase-noise from low intensity areas was suppressed by weighing the absolute flow values with their intensity values. The retinal flow en-face image shows blood flow at locations that match with the vascular structure shown in the intensity en-face image. The smaller vessels branches are however difficult to distinguish from the background due to their small blood flow velocity and small cross-sectional areas.

Equivalent en-face images of the choroidal intensity (Fig. 8D) and flow (Fig. 8E) were made by integration over depth for the area below the RPE. The choroidal intensity en-face image shows predominantly the larger deeper lying choroidal vasculature as large structures with low intensity. The retinal vasculature can be seen as shadows in this image. The choroidal flow en-face image however shows a different vasculature existing of the smaller choroidal vessels which are located directly below the retinal pigment epithelium. The explanation of the difference between the two en-face images can be found in the observed intensity and flow velocity for both vascular structures. The large choroidal vessels have a substantial lower intensity than the surrounding structures, which makes them visible in the intensity en-face image. The observed flow velocity for the large choroidal vessels is however low and almost equivalent to the background noise, which makes these vessels not visible in

#150555 - $15.00 USD Received 5 Jul 2011; revised 10 Sep 2011; accepted 17 Sep 2011; published 5 Oct 2011

the flow en-face image. This is exactly the opposite for the small choroidal vessels. The flow signal also fluctuates due to the cardiac cycle and changes in blood vessel orientation. Consequently in some sections of the flow en-face image the flow signal is more difficult to observe or absent. Nevertheless it is possible to differentiate perfused areas from non-perfused areas. The full data set is viewable as a movie in Fig. 8.

The visualization of a different part of the choroidal vasculature by phase-resolved OFDI is potentially interesting in the evaluation of pathology.

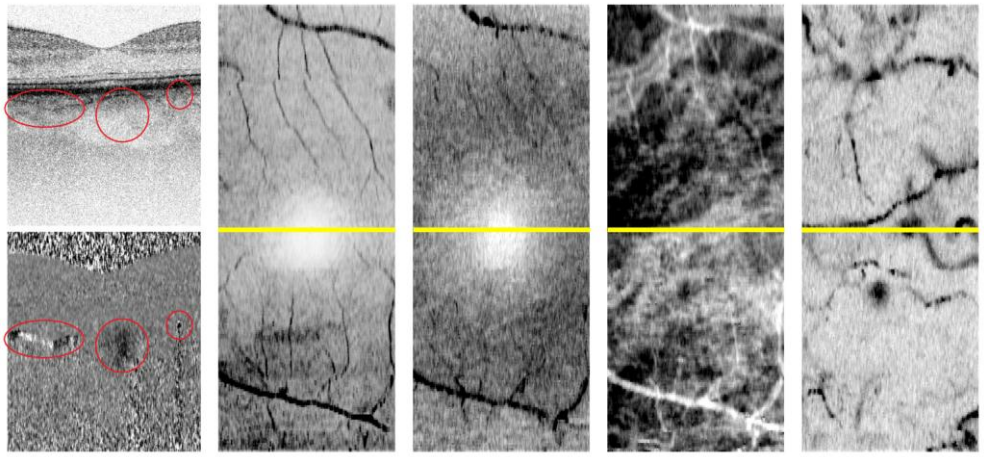

Fig. 8. Movie of the flow imaging of the macula of a healthy volunteer with (A) cross-sectional images of the intensity (top) and bi-directional flow (bottom) (displayed depth is 1.5 mm) and en-face images of (B) the retinal intensity, (C) the retinal blood flow, (D) the choroidal intensity, and (E) the choroidal flow. The red ellipses (not in movie) indicate areas with blood flow in the cross-sectional images, and the yellow line indicates the position of the cross-sectional images in the en-face images. Movie-file locations: Media 1 low-resolution (3.67 MB) and Media 2 high-resolution (13.0 MB).

5.4 Flow imaging after a RPE and choroid transplantation treatment

We demonstrate the clinical relevance of phase-resolved OFDI by the in-vivo measurement of blood flow in a patient with exudative age-related macular degeneration (AMD) after treatment with a RPE and choroid transplantation procedure. This treatment is used as a last resort to restore the vision of AMD patients where other treatments failed or could not be applied. During the transplantation procedure pathological RPE and choroid tissue is surgically removed below the macula and replaced by healthy tissue [17,18]. The healthy tissue patch, also called the graft, consists of RPE and choroid tissue obtained from a peripheral location in the patient's own eye. After the surgery the eye is filled with silicone oil that acts as a tamponade to close the retinal wounds and to prevent further hemorrhage. The success of this treatment is highly dependent on the ability of the graft to regain its function. This only happens if the blood perfusion within the graft is restored by revascularization and reconnection to the vascular network of the surrounding (original) choroid. Demonstration of blood flow within the graft would therefore be an important parameter to evaluate the success of the surgery.

A 87 year old female with AMD was imaged six weeks after treatment with a RPE and choroid transplantation. An auto-fluorescence photo (Heidelberg Retina Angiograph, Heidelberg Engineering, Heidelberg, Germany) was taken to show an overview of the transplantation site (Fig. 9A). The graft is visible as a light patch covering the macular region. In the upper-right corner a dark area can be seen from where the graft tissue was taken. The 1-µm OFDI system was used with 10 times averaging to show the cross-sectional anatomy of the transplantation site (Fig. 9B). The graft (G) is visible as a large tissue lump below the

#150555 - $15.00 USD Received 5 Jul 2011; revised 10 Sep 2011; accepted 17 Sep 2011; published 5 Oct 2011

retina and displaced the fovea (F) from its original location. The graft lies on top of the remnants of the original choroid (C), but is partially separated by a sub-graft fluid space (S).

Blood flow within the graft was evaluated by phase-resolved OFDI imaging of the center part of the graft for which the acquisition and data processing was done as described for the healthy volunteer in section 5.3. The area for which flow imaging is performed is indicated by a red square in Fig. 9A and by a red arrow in Fig. 9B. In Fig. 10 the results are shown, which are animated in a movie. The bi-directional flow image (Fig. 10A, bottom) shows blood flow that is located within the graft just below the RPE in the intensity cross-sectional image (Fig. 10A, top). The structure of the retinal vasculature is shown in the retinal intensity en-face image (Fig. 10B) and appears similar as for a healthy person. The intensity distribution in this image is however not uniform due to changes in the retinal reflectivity and folds in the graft which cause changes in the retinal thickness. A similar effect can be seen in the retinal flow en-face image (Fig. 10C) where the local change in retinal thickness creates shadowlike artifacts. Nevertheless retinal flow is observed for the large retinal vessel in the lower section of the image. Flow in the smaller retinal vessels is however not observed. The intensity en-face image of the choroid (Fig. 10D) shows that the perfusion observed in the bi-directional flow image originates from a dense network of parallel ladder-like vessels. Although this type of choroidal vasculature is normally not found below the macula, it is characteristic for the peripheral location where the graft was obtained [17,49]. In the lower part of this en-face image a shadow can be seen from the large retinal vessel. The choroidal flow en-face image (Fig. 10E) shows the measured flow in the graft as vertically oriented broken lines. The flow matches well the observed structure in the intensity en-face image for which an example is indicated by red triangles. The discontinuities in the measured flow are attributed to eye-motion artifacts, pulsatile blood flow, and changes in blood vessel orientation. The observed blood flow indicates (partial) reperfusion of the graft and gives therefore a good indication of successful surgery.

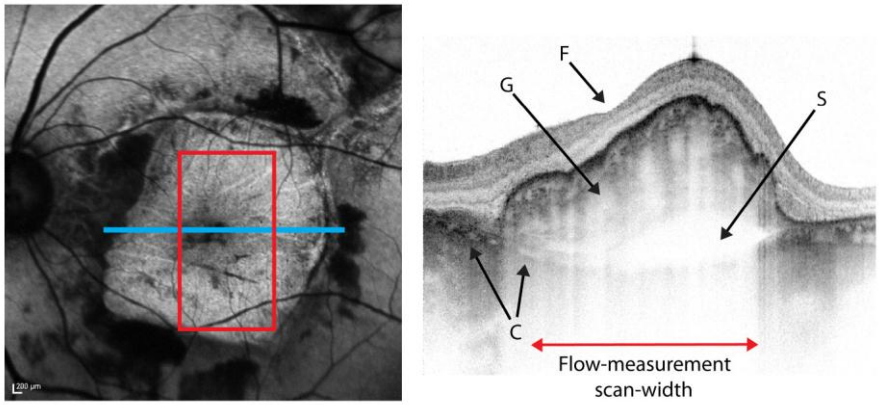

Fig. 9. (A) Auto-fluorescence photo of the retina with the graft as a light patch covering the macular region (8.26 mm x 8.26 mm). A part of the original location of the graft can be seen as a dark area in the upper right corner. In blue the location of the cross-sectional image is indicated and in red the area for flow imaging is marked. (B) 1-µm OFDI cross-sectional image (width 4.4 mm, height 2.5 mm) of the graft with arrows indicating the original choroid (**C**), the fovea (**F**), the transplantation graft (**G**), and sub-graft fluid (**S**). The flow imaging area is indicated by a red arrow.

#150555 - $15.00 USD Received 5 Jul 2011; revised 10 Sep 2011; accepted 17 Sep 2011; published 5 Oct 2011

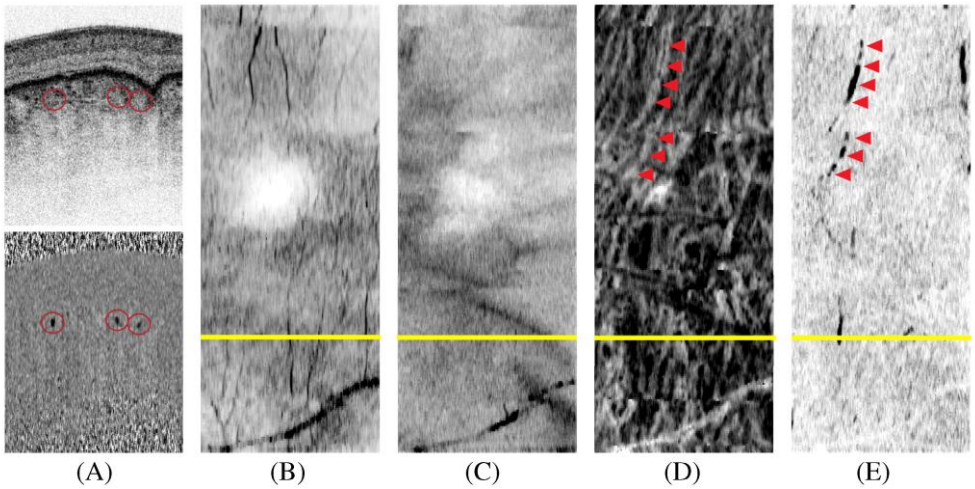

Fig. 10. Movie of the flow imaging of the center part of the graft with (A) cross-sectional images of the intensity (top) and bi-directional flow (bottom) (depth-span is 1.5 mm) and en-face images of (B) the retinal intensity, (C) the retinal blood flow, (D) the choroidal (graft) intensity, and (E) the choroidal (graft) flow. The red ellipses (not in movie) indicate areas with blood flow in the cross-sectional images, the red triangles match the structure and the blood flow of a particular vessel in the choroidal en-face images, and the yellow lines indicates the position of the cross-sectional images in the en-face images. Movie-file locations: Media 3 low-resolution (3.67 MB) and Media 4 high-resolution (13.0 MB).

6. Conclusion

In conclusion, we have demonstrated phase-stabilization of an OFDI system by a new post-processing algorithm. We reached shot-noise limited performance within 1 dB and demonstrated the advantage of phase-stabilization over non-stabilized data-processing by the removal of fixed-pattern noise artifacts and artifact-free in-vivo phase-resolved OFDI imaging of blood flow in the human choroid. We showed in a healthy eye that phase-resolved imaging is able to reveal a network of smaller choroidal vessels in the macula that was not visible in intensity images. The clinical potential of this technology was shown by the first demonstration of in vivo measurement of blood flow in a transplanted tissue graft. This first demonstration shows that phase-resolved OFDI has the potential to evaluate transplantation surgery in the posterior segment of the human eye.

Acknowledgments

This research was supported by grants from Stichting Wetenschappelijk Onderzoek Oogziekenhuis (SWOO) Prof. Dr. H.J. Flieringa, Combined Ophthalmic Research Rotterdam (CORR), and the Dutch MS Research Foundation.

#150555 - $15.00 USD Received 5 Jul 2011; revised 10 Sep 2011; accepted 17 Sep 2011; published 5 Oct 2011